In situ observation of compressive deformation of an interconnected network of zinc oxide tetrapods

Eloise Veys [a], Louis Makower [a], Marcus Williamson [a], Lena M. Saure [b], Rainer Adelung [b], Fabian Schütt [b], Nicola M. Pugno [c,d,a], Thomas James Marrow [a,*]

[a] Department of Materials, University of Oxford, Parks Rd, Oxford OX1 3PH, United Kingdom
[b] Faculty of Engineering, Kiel University, Kaiserstraße 2, Kiel 24143, Germany
[c] Department of Civil, Environmental and Mechanical Engineering, Laboratory of Bioinspired, Bionic, Nano, Meta Materials & Mechanics, University of Trento, via Mesiano, 77, Trento 38123, Italy
[d] School of Engineering and Materials Science, Queen Mary University of London, Mile End Road, London E1 4NS, United Kingdom

ABSTRACT

Zinc oxide tetrapods have remarkable functional and mechanical properties with potential applications in different fields including nanoelectronic and optoelectronic sensing, functional composites and coatings, as well as energy harvesting and storage. Based on the 3D shape of these microparticles, they can be assembled into highly porous (up to 98%) macroscopic ceramic framework structures that can be utilized as a versatile template for the fabrication of other multi-scaled foam-like materials. Here we investigated the three-dimensional structure of low density interconnected zinc oxide tetrapod networks by high resolution X-ray computed tomography. *In situ* observations during mechanical loading show inhomogeneous development of anelastic strain (damage) during compression, and homogeneous elastic recovery on unloading. Individual tetrapods are observed to deform by arm rotation to accommodate strain.

Zinc oxide (ZnO) is a semi-conducting metal oxide with remarkable functional properties including piezo-electricity and opto-electricity due to its large band gap and hexagonal-wurtzite crystal structure as well as good mechanical and thermal properties [1]. It can be grown in a variety of micro- and nanostructures of which one prominent shape is a three-dimensional (3D) tetrapod geometry of four arms connected at a central core [1,2]. It has already been demonstrated that nano and micro-scale tetrapods of ZnO (t-ZnO) have widespread potential applications in many fields, including biomedical engineering in the form of functional composites, optoelectronic and nanoelectronics sensing, energy harvesting and storage, as well as in environmental remediation [1]. Furthermore, tetrapodal particles can be further assembled into highly porous (up to 98%) macroscopic ceramic framework structures, providing a very high free volume as the spatially extended arms of the tetrapods prohibit efficient close packing. These interconnected networks offer easy access to active surfaces in a mechanically stable, compliant and low-density structure [2] and can be further utilized as a versatile template for the fabrication of other multi-scaled foam-like materials, so-called aeromaterials, from different 1D and 2D nanomaterials, such as graphene, hexagonal boron nitride, as well as carbon

nanotubes [3,4]. These freestanding aeromaterials are ultra-lightweight, with densities in the order of only a few mg/cm^3 and are characterized by a unique set of mechanical, electrical and optical properties [4,5].

The low nominal elastic moduli of such interconnected networks are very favourable for flexible electronics and mechanically robust sensors [6], but there is limited knowledge of the relationships between network architecture and properties, nor how these degrade with mechanical damage such as from cyclic loading [7]. This is needed to design functional materials with optimal properties and prolonged lifetimes. Novel micromechanical studies of the hinging and buckling deformation of individual aero-graphite tetrapods [8] provided insights into how they may behave collectively as self-assembled networks [4]. However, there have been no such studies of functional ceramics such as t-ZnO, although both the elastic modulus and electrical conductivity have been observed to decrease as network connections change when the elastic limit is exceeded [9].

Here we characterise the 3D network of interconnected t-ZnO using high resolution X-ray computed tomography (μXCT) to quantify the tetrapods' geometry and distribution. *In situ* μXCT observations during mechanical loading allow deformation within the bulk material to be
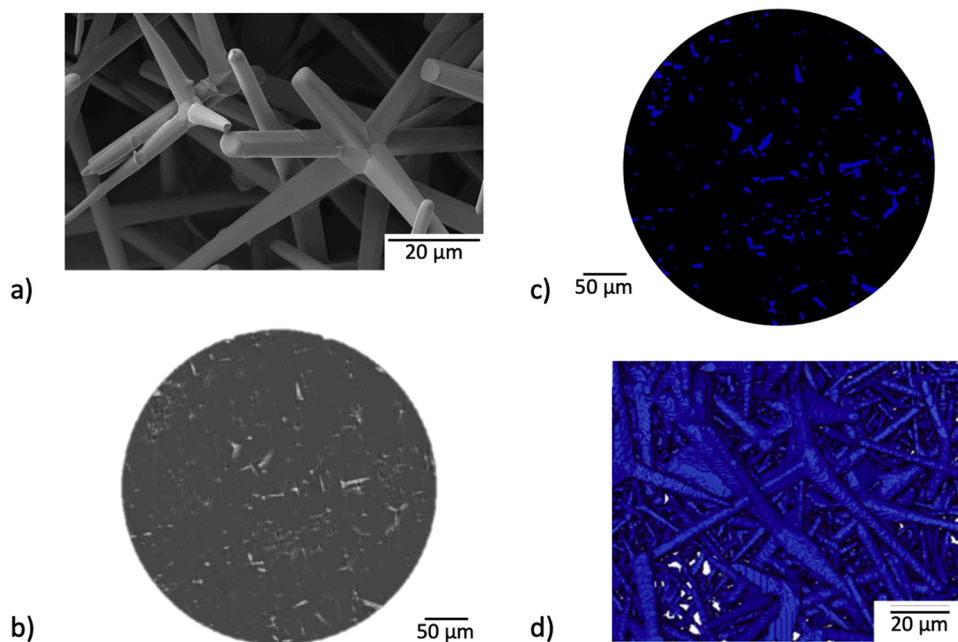

Fig. 1. Visualisation of the t-ZnO network (0.3 g cm^{-3} density): (a) scanning electron microscopy; (b) cross-sectional orthoslice of tomograph (after filters to reduce noise); (c) threshold segmented orthoslice; (d) 3D rendering of a tomographed region (after segmentation).
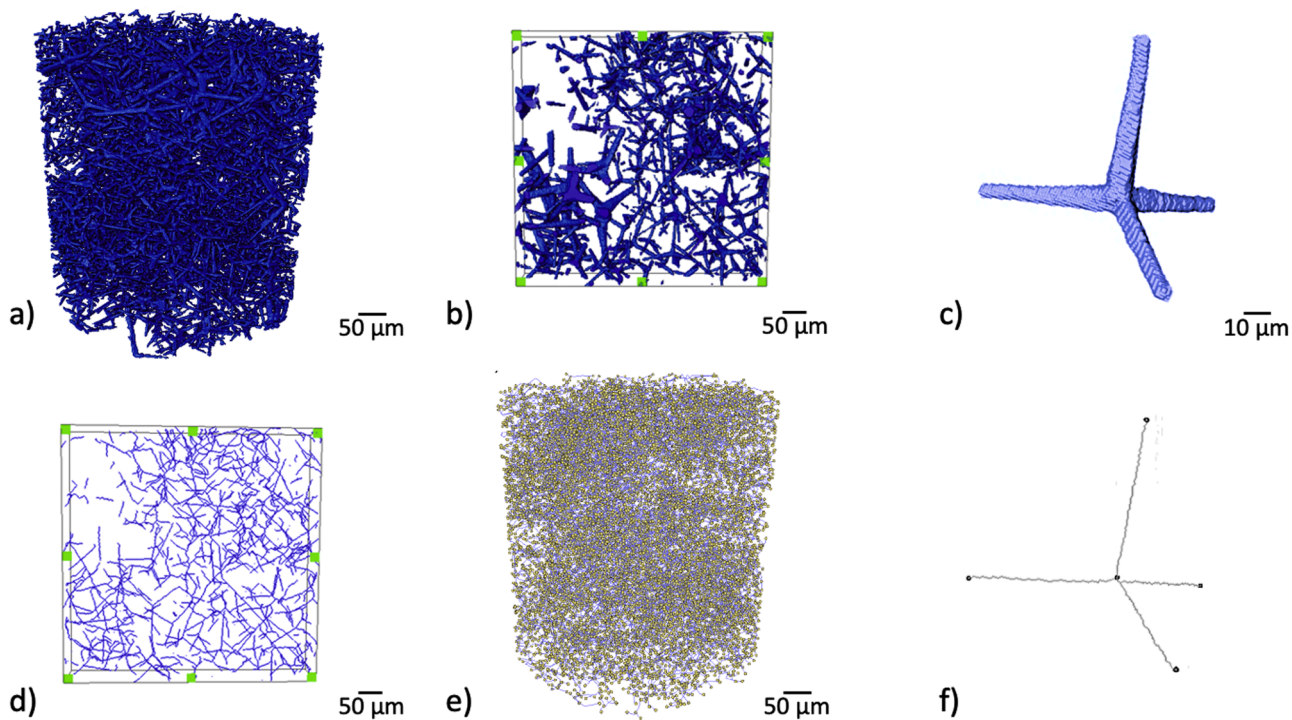

Fig. 2. Skeletonisation of the t-ZnO network (0.3 g cm^{-3} density): (a) visualisation of the tomographed region of interest after labelling; (b) tetrapods in a subregion of the same volume; (c) a single tetrapod; (d) the subregion after skeletonization (ligaments only shown); (e) tomographed region of interest after skeletonization (ligaments and nodes shown); (f) the skeletonised single tetrapod with ligaments and nodes.

examined, for the first time.

The t-ZnO material was produced via flame transport synthesis with post-synthesis compression and sintering [9]. Briefly, zinc microparticles (size 1–10 µm) were mixed with polyvinyl butyral (mass ratio 1:2) and heated for 30 min at 900 °C to produce a loose t-ZnO powder. Different masses were compressed in a ceramic mould (3 mm height, 3 mm diameter) to form pellets that were heated (unconstrained) at

1150 °C for 5 h to obtain specimens with nominal bulk densities between 0.3 and 0.9 g cm^{-3}. Scanning electron microscopy (Zeiss NVision 40 SEM, operating at 5 kV with a ~10 nm carbon coating) (Fig. 1a) confirmed the characteristic network architecture of interconnected tetrapods [10].

3D characterisation was done by µXCT (Zeiss Xradia Versa 610 microscope, operating between 60 and 120 kV with voxel size from 1 to
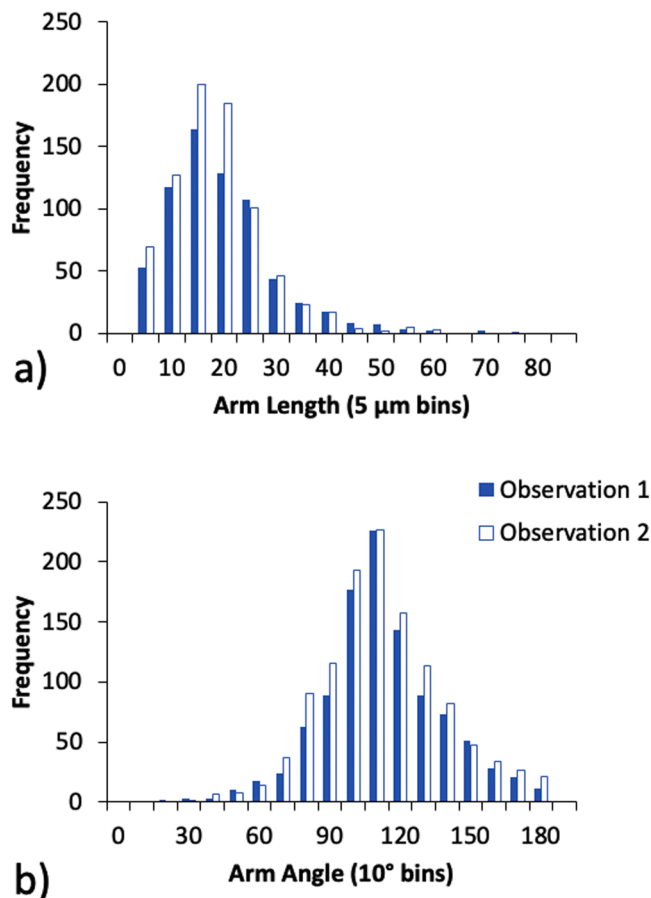
Fig. 3. Distributions of arm lengths and inter-arm angles measured by skeletonization of tomographs of t-ZnO with 0.3 g cm^{-3} density. Observation 1 and 2 were at 5 and 10% nominal strain, and show no significant difference.

1.7 μm) using the instrument software for attenuation contrast image reconstruction. Post-processing and analysis of the tomographs was done using the Avizo Fire software (*v.2020.3.1*). A Non-Local Means Filter was applied before intensity-based segmentation of the higher attenuation ZnO (Fig. 1b–d). Tomographs at 1.7 μm per voxel were sufficient to resolve the t-ZnO structure, though volume and surface measurements of the tetrapods by image segmentation have a subjective bias; the partial volume effect [11] is significant because the t-ZnO arms have cross-section dimensions (~1–3 μm) comparable to the image voxel size [3]. All samples were quite homogeneous; the observed solid fraction of ZnO within the sample volume (a moving cube of ~300 μm side) was constant both radially and axially (variance <15%) for all densities. Precise measurement of the total volume (±0.001 cm^3) via image texture classification to determine the sample's external boundaries, and of its mass using an A&D GH-202 balance (±0.01 mg) gave true densities of 0.29 ± 0.01, 0.41 ± 0.01, 0.52 ± 0.01 and 0.74 ± 0.01 g cm^{-3} for "nominal" densities of 0.3, 0.45, 0.6 and 0.9 g cm^{-3} respectively. The difference, which indicates expansion of the pellets, is greater for the higher density materials and is deduced to arise from interactions between the tetrapods after compression during processing.

To quantify the structure of the tetrapod network (Fig. 2a and b) a thinning algorithm [12] can be applied to the segmented image to determine its medial axis skeleton, which is described as a set of nodes connected by ligaments (1 voxel thickness) that are equidistant from the surfaces of the solid (Fig. 2d and e). Dead-end branches with length fewer than 5 voxels were regarded as noise and removed. This allowed measurement of arm lengths (between connected nodes) and interarm angles (between pairs of arms with common nodes). This skeletonization generally, and incorrectly, resolved the centers of tetrapods as 2 closely

adjacent nodes (1 or 2 voxel separation) instead of a single node. An example tetrapod, from a 0.3 g cm^{-3} sample tomographed at 1 μm voxel, is shown in Fig. 2c. Its skeleton (Fig. 2f) has a pair of 3-coordinated nodes at its center that have been joined for visualisation. Considering this double-counting, the number of tetrapods within a reconstructed volume of ~0.05 mm^3 was estimated at ~3000, i.e., a number density of ~ 6×10^4 mm^{-3}. The general network characteristics were insensitive to deformation (Fig. 3); in successive compressive observations (5 and 10% nominal strain) the mean arm lengths (Fig. 3a) were 17.4 μm (standard error in the mean 0.4 μm, standard deviation 11 μm) and 16.0 μm (standard error in the mean 0.3 μm, standard deviation 9.2 μm) respectively. The interarm angle distributions were also similar (Fig. 3b) at 107.0° (standard error in the mean 0.8°, standard deviation 25.7°) and 107.4° (standard error in the mean 0.8°, standard deviation 26.0°) respectively. The mean angle is close to the theoretical angle of ~110° [13]. The observed range illustrates the lack of perfect symmetry that arises from lattice strains during crystal growth [9] and is consistent with electron microscopy of t-ZnO structures produced by chemical vapour deposition [14].

To examine the deformation of the t-ZnO network in more detail, *in situ* XCT observations at 0.7 μm voxel were performed of a 0.45 g cm^{-3} sample, which was mounted in an X-ray transparent PMMA load-bearing tube and compressed between PTFE anvils by sequential displacements of ~75 μm applied via a manually controlled micrometer. The nominal strain over the sample length (3 mm) was estimated by μXCT observation of the change in anvil separation. Incremental global digital volume correlation (gDVC), which converged for mesh sizes of 100–250 μm, was applied using *Avizo*, whereby the tomograph at each step was correlated with the reference tomograph of the previous step. The incremental displacement vector fields were summed to obtain the cumulative three-dimensional displacements. Further details are summarised in the supplementary information. As an example, Fig. 4a is a vertical section of the residual field at 8.7% nominal strain. The residual field [15] quantifies the difference between the second image and the reference, where the latter has been deformed by the gDVC-calculated displacement field; large residuals (i.e., high contrast in this visualisation) indicate poor correlation, which can be caused by local changes in the image (i.e., the structure of the material). Significant residuals were observed close to the moving anvil within a region where the mean displacements were large and of high variability (Fig. 4b); the size of this region increased with applied nominal strain. This region of poor correlation and large displacements demonstrates significant and local changes to the network structure. In the lower part of the sample, where low residuals indicated accurate displacement measurement and no significant changes in structure, the displacement gradient (i.e., strain) increased with the applied strain. The measured strain in the lower region was less than the applied strain, due to accommodation of the displacement of the moving anvil in the upper region, and increased in magnitude as the high residual region was approached (Fig. 4c), showing nonlinear material behavior with increasing deformation. However, similar behavior was observed on unloading in both regions; when the 0.45 g cm^{-3} sample was unloaded by 2.4% nominal strain from a compressive nominal strain of 8.7%, the gDVC analysis measured a uniform strain relaxation of 2.5 ± 0.2% with low residuals over the entire sample. Such reversible behavior is quite like the compaction of a granular solid [16] in which *in situ* observations have also shown anelastic deformation to localize at the contacting surface [17,18].

The electrical conductivity of a t-ZnO network (density ~0.115 g cm^{-3}) has been observed to increase and then decrease with compression [9], which was attributed to improved tetrapod contact with increasing strain and then disruption of the network; the applied deformation indicated an elastic limit of ~2% nominal strain. Inspection of Fig. 4c shows the transition between the high correlation and low correlation regions is at local strain of ~0.5–1%. This lower elastic limit may be due to the higher network density of this 0.45 g cm^{-3} sample.

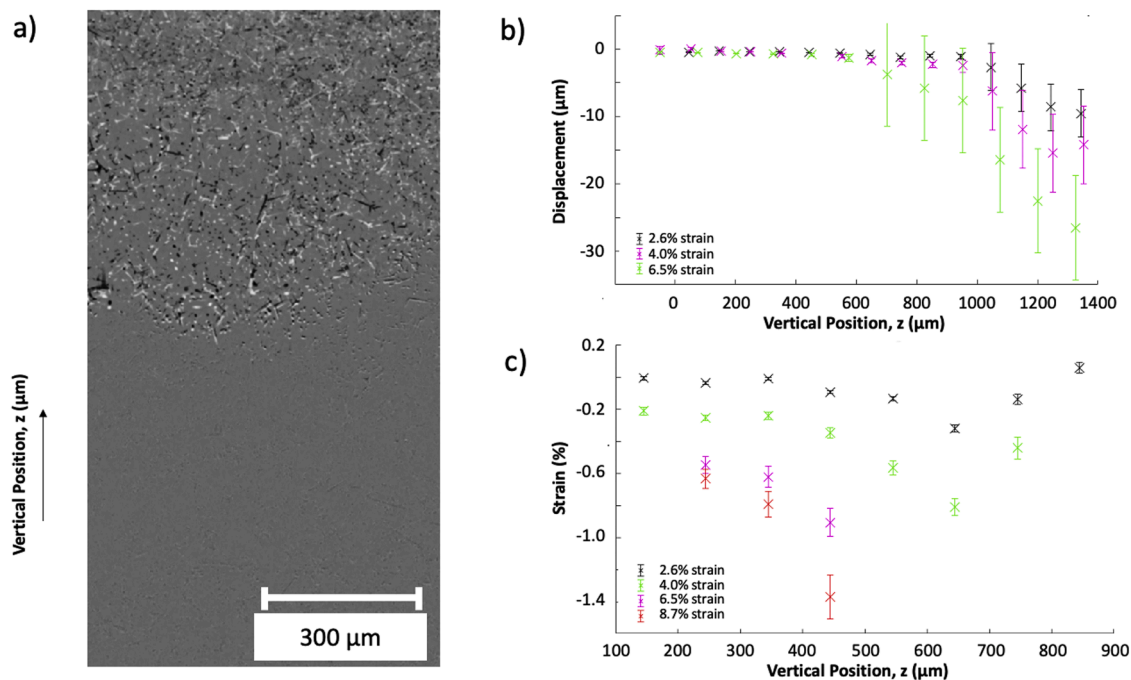The mechanism by which the network structure accommodates

Fig. 4. Measurement of deformation in t-ZnO (0.45 g cm^{-3} density) by global digital volume correlation of computed X-ray tomographs; (a) the residual field at 8.7% nominal strain; (b) vertical displacement with distance from the bottom of the sample at different nominal strains (data at 8.7% strain are not shown due to the high residuals); (c) vertical strain (in the region of low residuals) with distance from the bottom of the sample at different nominal strains. The fixed anvil is at the lower surface (z~0).
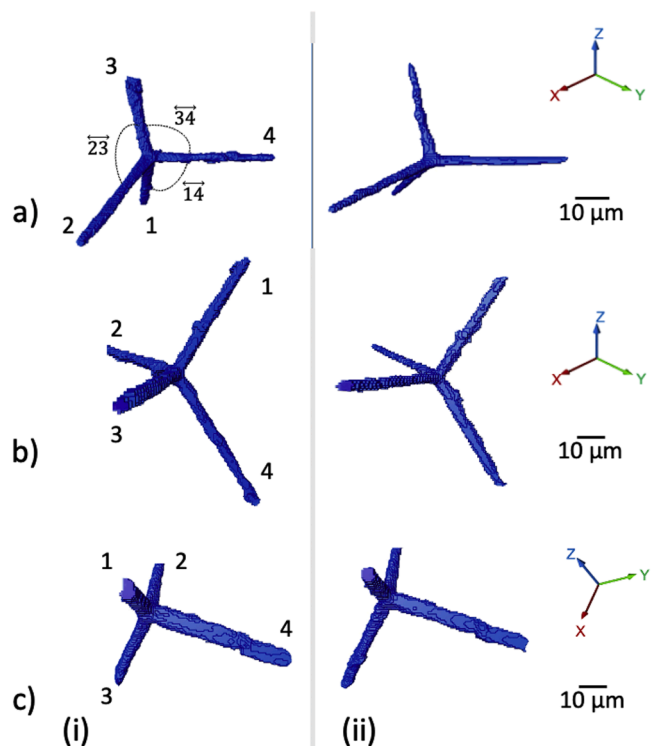

Fig. 5. Visualisation of t-ZnO tetrapods a) to c) from (i) observation 1 at 5% nominal strain and (ii) observation 2 at 10% nominal strain in a network with 0.3 g cm^{-3} density. The anvil compression direction between *in situ* observations was parallel to the Z-axis. Arms 1–4 are labelled, where 34 is the angle between arms 3 and 4, etc.

Table 1

Inter-arm angles (°) measured for tetrapod examples (a)–(c) (see Fig. 5) at (i) observation 1 at 5% nominal compressive strain and (ii) observation 2 at 10% nominal strain in t-ZnO with 0.3 g cm^{-3} density. 12 is the angle between arms 1 and 2, etc. Significant changes are highlighted in bold.

		12	13	14	23	24	34
a)	(i)	115 ± 2	131 ± 5	103 ± 1	100 ± 1	102 ± 1	101 ± 1
	(ii)	101 ± 2	102 ± 2	117 ± 3	102 ± 2	127 ± 5	103 ± 2
b)	(i)	99 ± 3	131 ± 6	110 ± 3	117 ± 6	98 ± 3	98 ± 2
	(ii)	97 ± 7	100 ± 2	106 ± 6	114 ± 9	119 ± 12	116 ± 7
c)	(i)	93 ± 2	128 ± 7	124 ± 7	109 ± 3	92 ± 3	102 ± 3
	(ii)	133 ± 13	87 ± 5	108 ± 7	116 ± 4	105 ± 3	103 ± 2

deformation was examined for individual tetrapods (Fig. 5) in a 0.3 g cm^{-3} sample that was observed *in situ* (at 1 μm voxel). The inter-arm angles of the same tetrapods were measured in successive observations at nominal compressive strains of approximately 5 and 10% (Table 1); i.e., where the bulk of the sample was beyond the elastic limit. Angular measurement errors were estimated conservatively using ± 2 μm and ± 1 μm uncertainty in the location of the central node and arm tip nodes. The first example (Fig. 5a) increased the inter-arm angles 14 and 24, and decreased 12 and 13 with increasing strain. This corresponds to rotation of arms 1 and 2 away from arm 4 and towards arm 3 and shows the tetrapod was compressed parallel to the loading axis. No bending of the arms could be observed. ZnO whiskers have a very high elastic limit [19] and it is assumed the deformation of the individual tetrapod arms may be similar to the elastic hinging behavior that has been observed in micromechanical testing of single arms of aero-graphite tetrapods [8]. Other t-ZnO examples (Fig. 5b and c) exhibited changes in shape that were less clearly aligned with the applied load. This indicates a quite complex mechanical interaction with adjacent structures, as has been predicted in interconnected tetrapod networks [4]. In the second example (Fig. 5b), arm 3 moved towards arm 1 largely by rotation about arm 2. In the third example (Fig. 5c), arm 1 rotated away from arm 2 towards arms 3 and 4.

In summary, we have shown that the network architecture of sintered t-ZnO can be observed by µXCT and quantified in a reproducible manner by image post-processing. *In situ* µXCT with gDVC finds significant and non-uniform deformation of the network structure with changes in the geometry of individual tetrapods. This observation is relevant to t-ZnO and also to materials for which it provides a template, such as aerographene [20] and aero-hBN [3,5]. Such deformation will affect how properties change at the elastic limit and the response of functional properties to cyclic fatigue, for example. µXCT may therefore be a very useful tool to study the interactions between deformation, microstructure and properties of functional network materials.

Declaration of Competing Interest

The authors declare that they have no known competing financial interests or personal relationships that could have appeared to influence the work reported in this paper.

Acknowledgments

Supplementary materials

Supplementary material associated with this article can be found, in the online version, at doi:10.1016/j.scriptamat.2022.115153.

References

[1] Y.K. Mishra, R. Adelung, ZnO tetrapod materials for functional applications, Mater. Today 21 (2018) 631–651, https://doi.org/10.1016/j.mattod.2017.11.003.

[2] G. Modi, Zinc oxide tetrapod: a morphology with multifunctional applications, Adv. Nat. Sci. Nanosci. Nanotechnol. 6 (2015) 33002, https://doi.org/10.1088/2043-6262/6/3/033002.

[3] F. Rasch, F. Schütt, L.M. Saure, S. Kaps, J. Strobel, O. Polonskyi, A.S. Nia, M. R. Lohe, Y.K. Mishra, F. Faupel, L. Kienle, X. Feng, R. Adelung, Wet-Chemical Assembly of 2D Nanomaterials into Lightweight, Microtube-Shaped, and Macroscopic 3D Networks, ACS Appl. Mater. Interfaces 11 (2019) 44652–44663, https://doi.org/10.1021/acsami.9b16565.

[4] F. Schütt, S. Signetti, H. Krüger, S. Röder, D. Smazna, S. Kaps, S.N. Gorb, Y. K. Mishra, N.M. Pugno, R. Adelung, Hierarchical self-entangled carbon nanotube tube networks, Nat. Commun. 8 (2017) 1215, https://doi.org/10.1038/s41467-017-01324-7.

[5] F. Schütt, M. Zapf, S. Signetti, J. Strobel, H. Krüger, R. Röder, J. Carstensen, N. Wolff, J. Marx, T. Carey, M. Schweichel, M.I. Terasa, L. Siebert, H.K. Hong, S. Kaps, B. Fiedler, Y.K. Mishra, Z. Lee, N.M. Pugno, L. Kienle, A.C. Ferrari, F. Torrisi, C. Ronning, R. Adelung, Conversionless efficient and broadband laser light diffusers for high brightness illumination applications, Nat. Commun. 11 (2020) 1437, https://doi.org/10.1038/s41467-020-14875-z.

[6] X. Tao, H. Jin, M. Mintken, N. Wolff, Y. Wang, R. Tao, Y. Li, H. Torun, J. Xie, J. Luo, J. Zhou, Q. Wu, S. Dong, J. Luo, L. Kienle, R. Adelung, Y.K. Mishra, Y.Q. Fu, Three-Dimensional Tetrapodal ZnO Microstructured Network Based Flexible Surface Acoustic Wave Device for Ultraviolet and Respiration Monitoring Applications, ACS Appl. Nano Mater. 3 (2020) 1468–1478, https://doi.org/10.1021/acsanm.9b02300.

[7] Z. Lin, X. Gui, Q. Gan, W. Chen, X. Cheng, M. Liu, Y. Zhu, Y. Yang, A. Cao, Z. Tang, In-Situ Welding Carbon Nanotubes into a Porous Solid with Super-High Compressive Strength and Fatigue Resistance, Sci. Rep. 5 (2015) 11336, https://doi.org/10.1038/srep11336.

[8] R. Meija, S. Signetti, A. Schuchardt, K. Meurisch, D. Smazna, M. Mecklenburg, K. Schulte, D. Erts, O. Lupan, B. Fiedler, Y.K. Mishra, R. Adelung, N.M. Pugno, Nanomechanics of individual aerographite tetrapods, Nat. Commun. 8 (2017) 14982, https://doi.org/10.1038/ncomms14982.

[9] Y.K. Mishra, S. Kaps, A. Schuchardt, I. Paulowicz, X. Jin, D. Gedamu, S. Freitag, M. Claus, S. Wille, A. Kovalev, S.N. Gorb, R. Adelung, Fabrication of Macroscopically Flexible and Highly Porous 3D Semiconductor Networks from Interpenetrating Nanostructures by a Simple Flame Transport Approach, Part. Part. Syst. Charact. 30 (2013) 775–783, https://doi.org/10.1002/ppsc.201300197.

[10] H.Y. Zahran, I.S. Yahia, Synthesis and characterization of ZnO tetrapods, Appl. Phys. A 119 (2015) 1397–1403, https://doi.org/10.1007/s00339-015-9112-5.

[11] D.B. Plewes, P.B. Dean, The influence of partial volume averaging on sphere detectability in computed tomography, Phys. Med. Biol. 26 (1981) 913–919, https://doi.org/10.1088/0031-9155/26/5/011.

[12] T.Y. Zhang, C.Y. Suen, A Fast Parallel Algorithm for Thinning Digital Patterns, Commun. ACM 27 (1984) 236–239, https://doi.org/10.1145/357994.358023.

[13] M. Shiojiri, C. Kaito, Structure and growth of ZnO smoke particles prepared by gas evaporation technique, J. Cryst. Growth 52 (1981) 173–177, https://doi.org/10.1016/0022-0248(81)90189-5.

[14] B.B. Wang, J.J. Xie, Q. Yuan, Y.P. Zhao, Growth mechanism and joint structure of {ZnO} tetrapods, J. Phys. D Appl. Phys. 41 (2008), 115153, https://doi.org/10.1088/0022-3727/41/10/102005.

[15] A. Buljac, C. Jailin, A. Mendoza, J. Neggers, T. Taillandier-Thomas, A. Bouterf, B. Smaniotto, F. Hild, S. Roux, Digital Volume Correlation: Review of Progress and Challenges, Exp. Mech. 58 (2018) 661–708, https://doi.org/10.1007/s11340-018-0390-7.

[16] R.C. Hurley, S.A. Hall, J.P. Wright, Multi-scale mechanics of granular solids from grain-resolved X-ray measurements, Proc. R. Soc. A Math. Phys. Eng. Sci. 473 (2017), 20170491, https://doi.org/10.1098/rspa.2017.0491.

[17] F. Forsberg, C.R. Siviour, 3D deformation and strain analysis in compacted sugar using x-ray microtomography and digital volume correlation, Meas. Sci. Technol. 20 (2009), 095703, https://doi.org/10.1088/0957-0233/20/9/095703.

[18] S.A. McDonald, L.C.R. Schneider, A.C.F. Cocks, P.J. Withers, Particle movement during the deep penetration of a granular material studied by X-ray microtomography, Scr. Mater. 54 (2006) 191–196, https://doi.org/10.1016/j.scriptamat.2005.09.042.

[19] R.B. Sharma, Deformation and Fracture of Zinc Oxide Whiskers, J. Appl. Phys. 41 (1970) 3371–3373, https://doi.org/10.1063/1.1659427.

[20] F. Schütt, F. Rasch, N. Deka, A. Reimers, L.M. Saure, S. Kaps, J. Rank, J. Carstensen, Y.K. Mishra, D. Misseroni, A.R. Vázquez, M.R. Lohe, A. Shaygan Nia, N.M. Pugno, X. Feng, R. Adelung, Electrically powered repeatable air explosions using microtubular graphene assemblies, Mater. Today 48 (2021) 7–17, https://doi.org/10.1016/j.mattod.2021.03.010.

Supplementary material: In situ observation of compressive deformation of an interconnected network of zinc oxide tetrapods

Digital Volume Correlation

The gDVC was performed using the Avizo fire software (2020.3.1). The volumetric data sets were first registered to the first step to ensure the DVC-computed displacement fields were all expressed in the same co-ordinate system.

To perform the DVC calculation, local DVC was first performed with a subset size of between 100-150 µm. The displacement field generated by this local technique was then used as a starting solution for a finite element based global DVC calculation. The mesh size used for these calculations varied from 100 µm for the first two calculations (i.e. step 1 - step 2 between 0 and 2.6% nominal strain and then step 2 - step 3 between 2.6% and 4.0% nominal strain), 125 µm for step 3-step 4 (i.e. 4.0 to 6.5% strain) and 225 µm for step 4-step 5 (i.e. 6.5% to 8.7% strain). The gDVC calculation is an iterative procedure, which converges to a solution when the difference between the displacement field of the nth and (n-1)[th] iteration is smaller than 10^{-3} voxels. Data for σ_η, the standard deviation of the normalised correlation residual, are reported in Table 1. The increase in σ_η is due to the development of the zone of high residuals.

Examples of the evolution of the residual fields are shown in Figure 1 to Figure 3. The figures are simple subtractions of the reference and subsequent image that has been transformed using the measured displacement field. They are presented using these same greyscale range. The pairing of white/dark features illustrates the failure of gDVC to adequately track displacements within the region of inelastic deformation at the contact with the moving anvil. This allows the boundary of the field to be identified.

Table 1: Data for σ_η, the standard deviation of the normalised correlation residual as a function of the applied strain (* rigid body motion of 10 µm between tomographs with 0% strain applied)

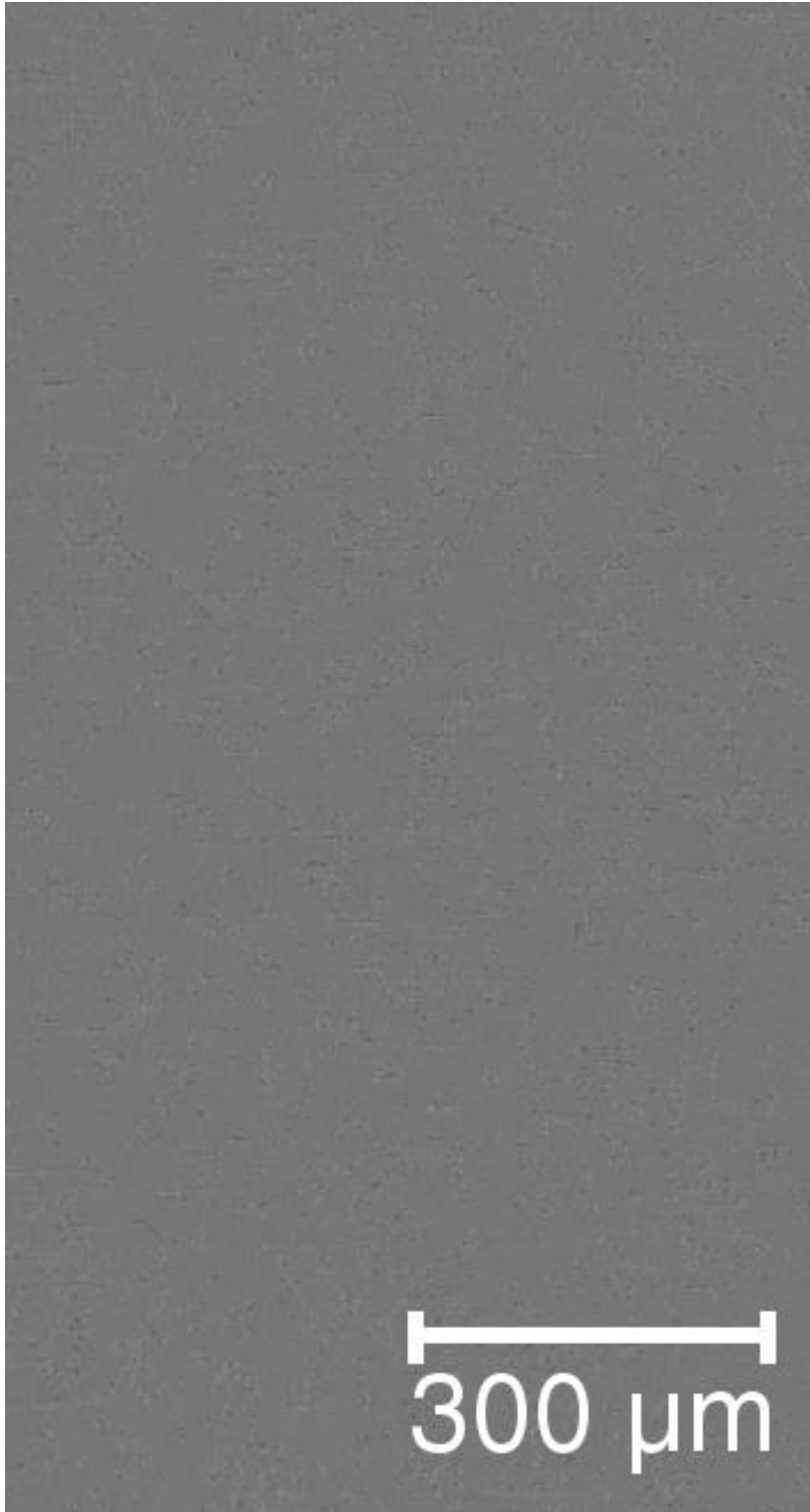| Change in nominal strain (%)	0*	2.6	1.3	2.5	2.2
Total nominal strain (%)	0	2.6	4.0	6.5	8.7
σ_η	0.012	0.017	0.020	0.024	0.039

Figure 1: Residuals for gDVC analysis of the displacements for a rigid body motion between tomographs of 10 µm
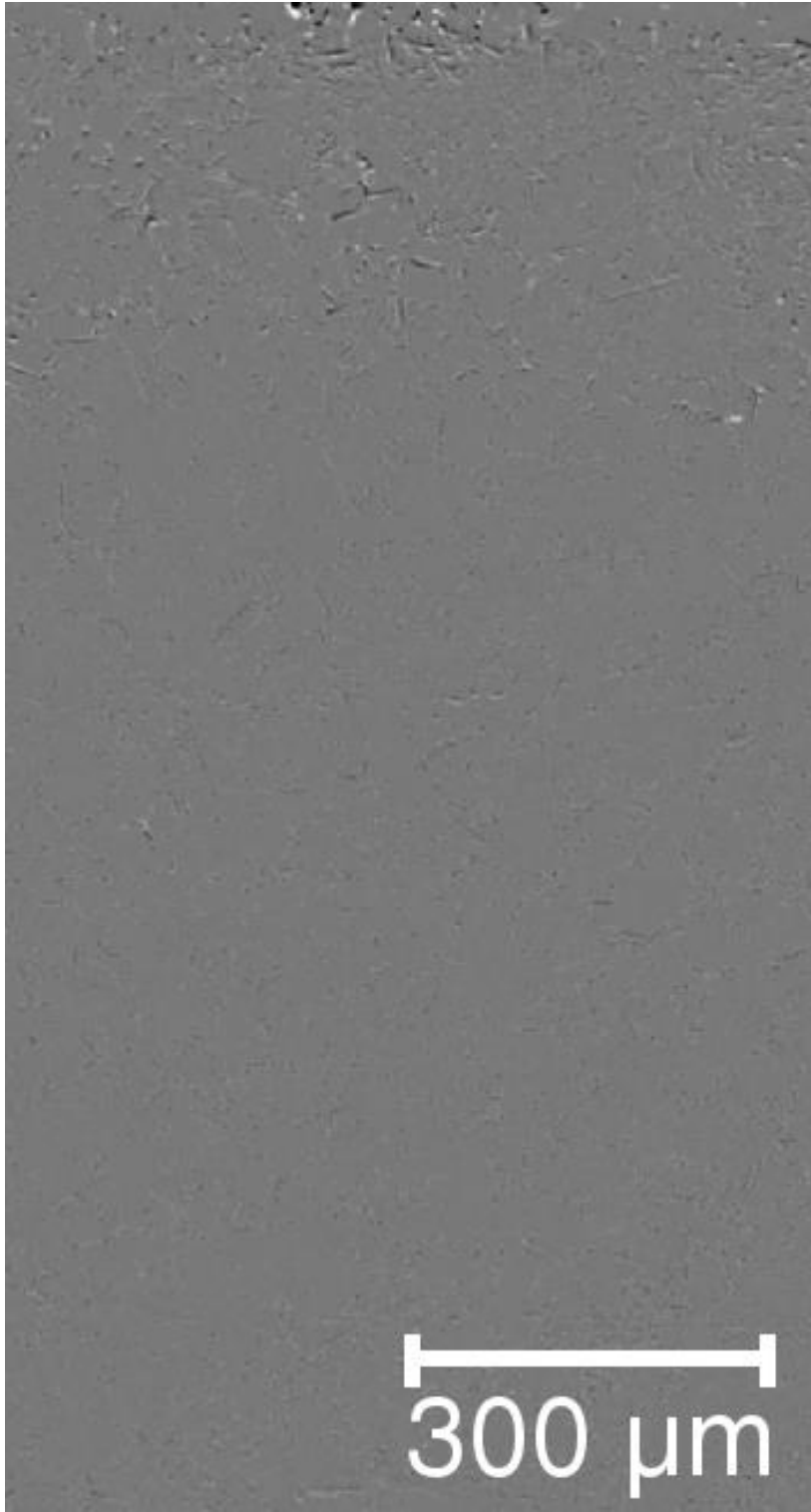
Figure 2: Residuals for gDVC analysis of the displacements for a nominal global strain of 2.6%
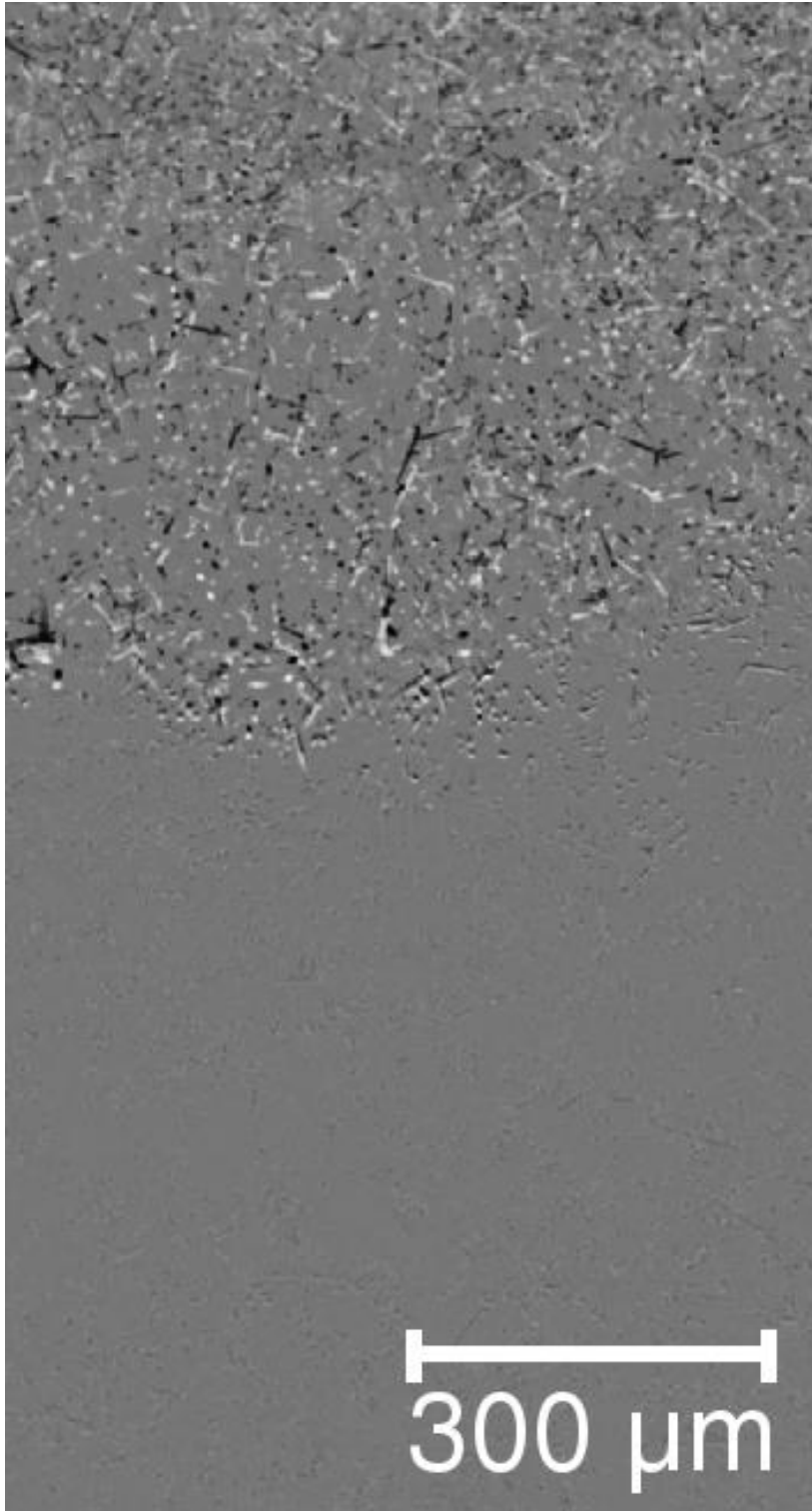
Figure 3: Residuals for gDVC analysis of the displacements at a total nominal global strain of 8.7%; data obtained by correlating the tomographs at 6.5% and 8.7% nominal strain.